Measuring the Magnetic and Hydrodynamic Properties of Assembled-MEMS Microrobots

Michael P. Kummer, Jake J. Abbott, Karl Vollmers, and Bradley J. Nelson

Institute of Robotics and Intelligent Systems

ETH Zurich, 8092 Zurich, Switzerland

e-mail: {kummerm, jabbott, kvollmers, bnelson}@ethz.ch

Abstract— **Microrobots experience physical phenomena that are difficult to model analytically and that are not completely captured with macro-scale prototypes. In this paper we present a reconfigurable robotic measurement system to characterize the magnetic and hydrodynamic properties of assembled-MEMS microrobots. The system consists of a powerful permanent magnet that is position controlled with a linear stage. The magnetic field is accurately characterized. Precision sensors are used to measure magnetic force as a function of applied field. The system is first used to validate an existing model for the magnetic force on a soft-magnetic ellipsoid. Next, the magnetic force on a soft-magnetic assembled-MEMS microrobot as a function of the applied field is measured experimentally. Finally, a vision tracking system is integrated with the setup to measure the hydrodynamic properties of the microrobot. The coefficient of viscous friction for the microrobot is obtained experimentally.**

I. INTRODUCTION

One approach to wireless control of microrobots is through externally applied magnetic fields. These untethered devices could navigate in bodily fluids to enable a number of new minimally invasive surgical and diagnostic procedures. Prior work by Yesin et al. [1] demonstrated that assembled-MEMS microrobots like that shown in Fig. 1 can be wirelessly controlled in a fluid environment. We are particularly interested in ophthalmic procedures to address disorders such as retinal-vein occlusion. Ophthalmic procedures will require the microrobot to navigate a viscoelastic fluid environment known as the vitreous humor [2]. For precise microrobot control, we must characterize the behavior of assembled-MEMS microrobots, being driven by external magnetic fields, through non-Newtonian (i.e. not purely viscous) fluid environments.

A common technique employed in microrobot design is to construct relatively large experimental prototypes, and then attempt to account for scaling effects. However, using this methodology, it is difficult to account for all of the important physical phenomena encountered at micro scales [3], or the increased difficulty in actually constructing the functioning microrobot. This makes the transition from large prototype to actual microrobot a difficult one. We are using an alternative methodology by designing, constructing, analyzing, and experimenting on actual assembled-MEMS microrobots.

Prior work in wireless magnetic manipulation has focused largely on the control of permanent magnets [4]–[8]. Our microrobot is constructed from soft-magnetic material, and
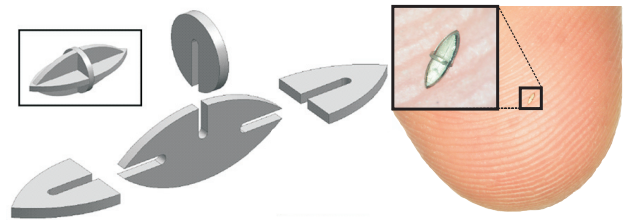

Fig. 1. An assembled-MEMS microrobot that is 800 μm long and 400 μm wide. The components are fabricated with electroplated nickel.

consequently, the magnetization of the material is a function of the applied field. Soft-magnetic materials provide easier fabrication and increased flexibility in microrobot control. Researchers have considered the control of soft-magnetic beads in viscous environments [9], where a spherical shape greatly simplifies the control problem. A magnetic model necessary for precise control of a non-spherical soft-magnetic body has only recently been developed [10].

Measuring the magnetic force on a soft-magnetic body placed in a magnetic field requires a custom experimental setup. In addition, we would like to understand the hydrodynamic properties of our microrobots in various fluid environments, including those which are non-Newtonian, under wireless magnetic actuation. These properties are only obtained accurately through experiment. In this paper we describe a custom experimental robotic system to investigate magnetization force and hydrodynamics of assembled-MEMS microrobots.

II. MEASURING MAGNETIC PROPERTIES

To measure the magnetic force acting on soft-magnetic microrobots as they move through a magnetic field, we have constructed a reconfigurable experimental setup, described in Section II-A. To understand the magnetic force on our microrobot, we require knowledge of the applied magnetic field, as well as the gradients in the field. This is discussed in Section II-B. The experimental setup is used to validate a known model in Section II-C. Finally, we measure the magnetic forces on an assembled-MEMS microrobot in Section II-D.
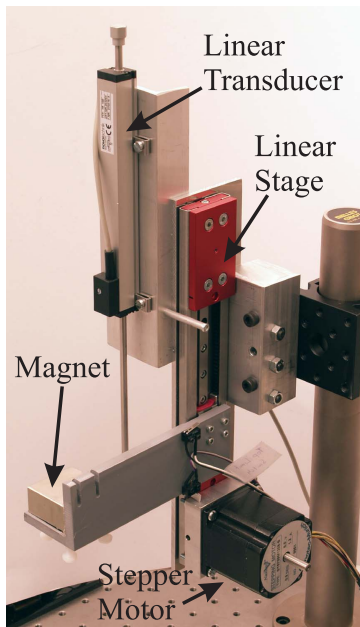
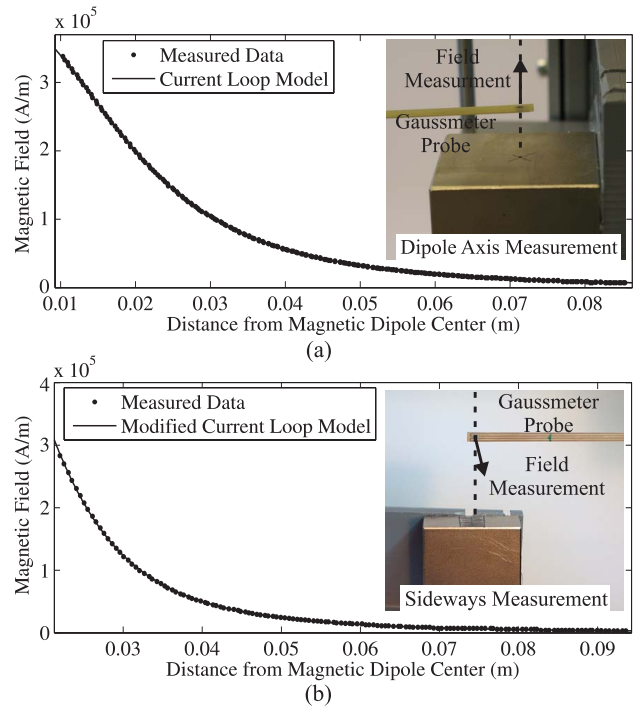Fig. 2. Linear stage to actuate the magnet in 1-DOF.

Fig. 3. Experimental magnetic field data measured along the dipole axis (a) and to the side (b) of a Q-40-40-20-N permanent magnet from SuperMagnete.ch.

A. Experimental Setup

All experiments involve a magnet moving along a single linear DOF. This component, common to all experiments, is shown in Fig. 2. We use a powerful Q-40-40-20-N permanent magnet from SuperMagnete.ch. The dimensions are $40 \times 40 \times 20$ mm, with the north and south poles on the two largest faces. The permanent magnet is rigidly mounted to an assembly with 1-DOF of travel along a linear stage. The magnet's displacement along the linear stage is controlled with a Nanotec ST5709M1208 high-torque stepper motor, driven by a Nanotec SMC42 current driver. The position of the magnet is measured with a Novotechnik TR100 position transducer, with a restoring spring to maintain contact with the magnet assembly. The position transducer has a travel of 100 mm. The entire measurement system is interfaced to a PC through an ELMICRO CardS12 microcontroller that performs the A/D conversion for the position transducer, controls the stepping frequency of the motor, and reads in the two limit switches which determine the end of travel of the magnet assembly. The microcontroller communicates with the PC through a serial port. The PC, running the Linux operating system, reads in user commands, implements the high-level control system, and collects data. For the remainder of this document, this setup will be referred to as the linear stage.

B. Characterizing the Magnetic Field

To characterize the magnetic field of the permanent magnet, we use a GM05 Gaussmeter from Hirst Magnetic Instruments. First, we measured the field along the dipole axis of the magnet as shown in the inset in Fig. 3(a). Second, we measured the component of the field parallel to the dipole axis, but measured along an axis perpendicular to the dipole axis and through the center of a side face of the magnet as

shown in the inset in Fig. 3(b). For each set of measurements, the Gaussmeter was fixed, and the magnet was moved along its range of travel by the linear stage.

It is desirable to fit a smoothly differentiable function to the magnetic field data, both for interpolation between measured values, as well as for the computation of field gradients, which are important to the generation of force on a magnetic moment. To model the field of a magnet, we can use a current loop model, where the dipole is created by a current loop of radius r with current i, resulting in a magnetic moment $|\mathbf{\Gamma}| = \pi i r^2$, with the direction of $\mathbf{\Gamma}$ defined by the right-hand rule [11]. The current model is most appropriate for modeling magnets whose dipole axis is the short dimension, as is the case for our magnet. There is no general analytical model for the field around a current loop [11], and although a far-field model is available [12], our permanent magnet has physical dimensions which are important to the field near the magnet. We can, however, calculate the magnitude of the field along the axis of the loop:

$$|\mathbf{H}| = \frac{|\mathbf{\Gamma}|}{c2\pi(r^2 + |\mathbf{P}|^2)^{3/2}} \quad (1)$$

in units of $\mathrm{A/m}$, where $\mathbf{P}$ is the vector from the dipole to the position of interest, and $c = 1$ (the inclusion of c will be discussed later). The direction of the field is defined by the current flow using the right-hand rule. This model loses validity for permanent magnets when r is large relative to $|\mathbf{P}|$. Once equipped with a differentiable model of the magnetic field along the dipole axis, we calculate the gradient

along the dipole axis as

$$\frac{d|\mathbf{H}|}{d|\mathbf{P}|} = -\frac{3|\mathbf{\Gamma}||\mathbf{P}|}{c2\pi(r^2 + |\mathbf{P}|^2)^{5/2}} \quad (2)$$

Figure 3(a) shows the magnetic-field data along the dipole axis of the magnet. Note that the left-most data point corresponds to the surface of the magnet. A current loop model was fit to the measured data using Matlab's Curve Fitting Toolbox. The model can be fit accurately ($R^2 = 0.9999$) to the entire data set with $|\mathbf{\Gamma}| = 29.36\,\mathrm{A \cdot m}^2$, $r = 22.83\,\mathrm{mm}$, and the center of the current loop located 7.251 mm below the magnet surface. It is clear from the figure that the fit is essentially perfect.

As with the field along the dipole axis, we require a differentiable model for the field to the side of the magnet. Comparison of (1) with the far-field model presented in [12] suggests that $c = 2$ in (1) and (2) may approximate the field and field gradient to the side of the magnet. Figure 3(b) shows the magnetic-field data measured to the side of the magnet. Note that the left-most data point is offset by 2 mm from the side surface due to the shape of the Gaussmeter probe. We find that the modified current loop model provides a fit with $R^2 = 0.9999$ for the sideways data, with the center of the current loop located at 1.038 cm below the magnet's side surface, $|\mathbf{\Gamma}| = 23.60\,\mathrm{A \cdot m}^2$, and $r = 14.04\,\mathrm{mm}$. Again, it is clear from the figure that the fit is essentially perfect.

C. Validating a Known Model

We have recently developed and experimentally verified a model for the magnetization of a small, soft-magnetic, axially symmetric body in an arbitrary magnetic field [10]. This magnetization is the source of magnetic torques and forces. It has been shown that many shapes can be accurately magnetically modeled by an equivalent ellipsoid [13], so an analysis of this shape provides insight into many others. The long axis of the body is referred to as the "easy axis" because it is the easiest direction to magnetize the body. A magnetic torque will tend to align the easy axis of the body with the applied field $\mathbf{H}$. In this paper, we will only investigate the case where the easy axis is aligned with the applied field.

Once equipped with a model of the magnetization vector $\mathbf{M}$ in the body from [10], we can compute the force on the body using the force on a magnetic dipole moment [11]:

$$\mathbf{F} = \mu_0 v \left(\mathbf{M} \cdot \nabla\right) \mathbf{H} \quad (3)$$

Since there is no electric current flowing through the region occupied by the body, Maxwell's equations provide that $\nabla \times \mathbf{H} = \mathbf{0}$. This allows us to express (3), after some manipulation, in a more intuitive form:

$$\mathbf{F} = \mu_0 v \begin{bmatrix} \mathbf{M} \cdot \frac{d}{dx}\mathbf{H} \\ \mathbf{M} \cdot \frac{d}{dy}\mathbf{H} \\ \mathbf{M} \cdot \frac{d}{dz}\mathbf{H} \end{bmatrix} \quad (4)$$

The first application of the measurement system is to validate the above magnetization force model. To that aim, we machined a prolate ellipsoid that is 4.90 mm long and 2.54 mm wide from HyMu 80 (80% Ni, 14.48% Fe, 5% Mo),
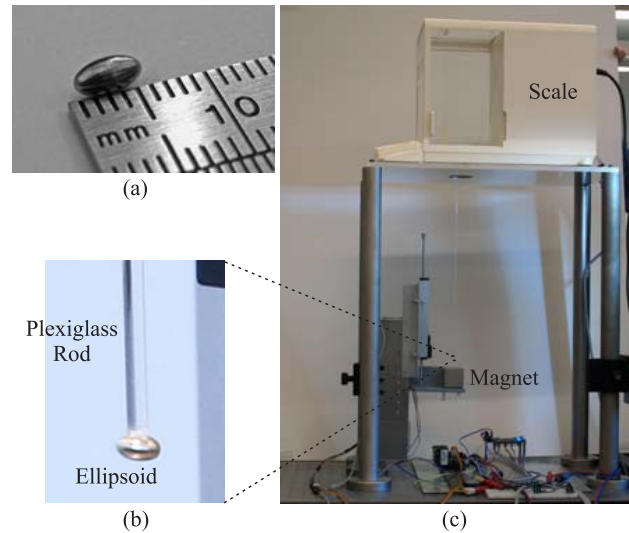

Fig. 4. (a) Machined ellipsoid of HyMu 80 that is 4.90 mm long and 2.54 mm wide. (b) The ellipsoid is attached to a plexiglass rod. (c) Setup to measure force on the ellipsoid. The plexiglass rod hangs the ellipsoid from a scale over the magnet.

a nearly ideal soft magnetic material. The ellipsoid is shown in Fig. 4(a). The density of HyMu 80 is $8700\,\mathrm{kg/m}^3$, and the mass was measured as 145.21 mg, giving a volume $v = 1.669 \times 10^{-8}\,\mathrm{m}^3$. We measured the saturation magnetization m_s of HyMu 80 with a vibrating-sample magnetometer (VSM) and found $m_s = 6.163 \times 10^5\,\mathrm{A/m}$ [10].

The ellipsoid is mounted to a long, thin plexiglass rod (see Fig. 4(b)) that is hung from an Ohaus Analytica Plus high precision scale (see Fig. 4(c)). The scale and linear stage are configured such that the center of the ellipsoid lies on the measurement axis of interest. To alleviate torque, the ellipsoid is always oriented such that its easy axis and the magnet field are parallel (Fig. 4(b) shows only one of two configurations used).

Figure 5(a) shows the measured magnetization force on the ellipsoid along the dipole axis, as well as the force predicted by the model. The position is reported from the dipole center, so the surface of the magnet corresponds to a position of 7.251 mm. Figure 5(b) shows the measured and predicted sideways magnetic force exerted on the ellipsoid. The side surface of the magnet corresponds to a position of 10.383 mm. We find that the model predicts the force on the ellipsoid well, for both sets of data. The bend that can be seen in the plots of the model represents the transition from unsaturated to saturated magnetization.

D. Microrobot Measurements

The microrobot we consider is made from nickel, which has a density of $8908\,\mathrm{kg/m}^3$, and has a measured mass of 1.90 mg. It has overall length and width dimensions of 2.5 mm and 1.25 mm, respectively, and the thickness of the individual components is 0.05 mm. The volume of the microrobot is calculated using the mass and density as $2.13 \times 10^{-10}\,\mathrm{m}^3$. We measured the magnetization of the microrobot along its long axis with a VSM [14] and the
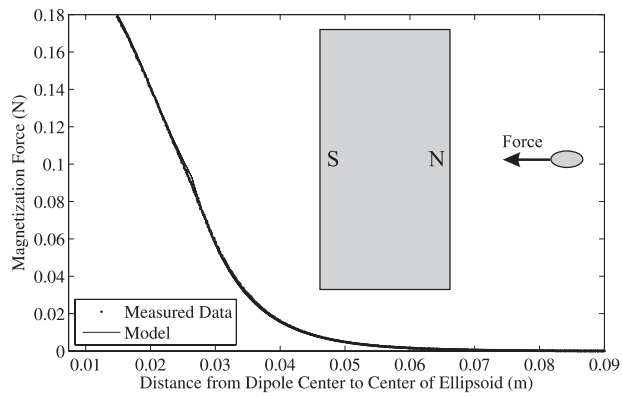
(a)
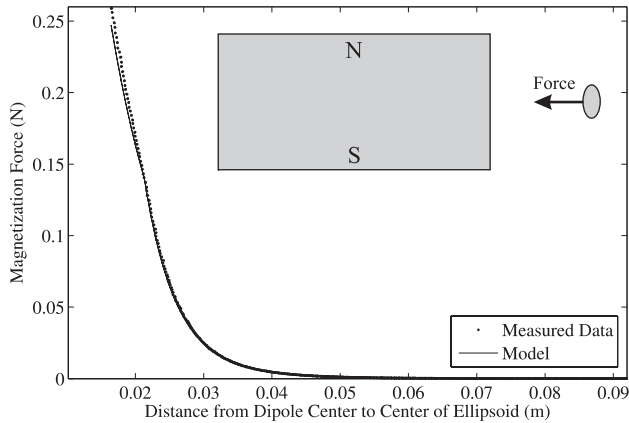
(b)

Fig. 5. Predicted and measured force (a) when approaching the ellipsoid along the dipole axis of the magnet and (b) when approaching the ellipsoid sideways. The inset illustrates the experimental setup, drawn with 1:1 scale to the data.
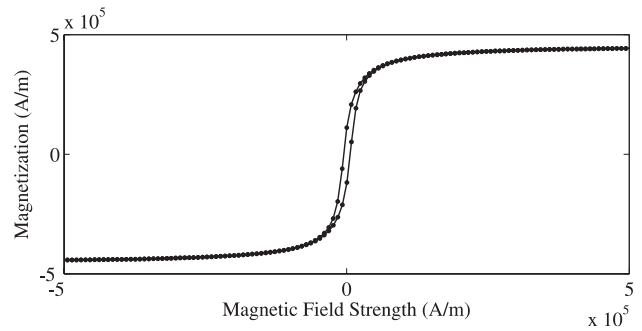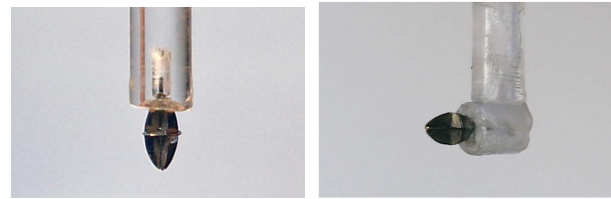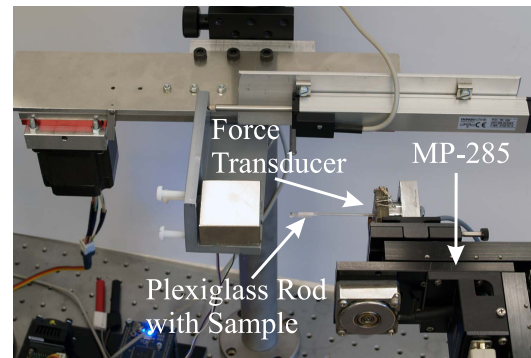

Fig. 6. VSM magnetization data of the microrobot along its long axis. The microrobot exhibits some hysteresis at low applied fields.

(a)   (b)

(c)

Fig. 7. Assembled-MEMS microrobot attached to plexiglass rod for force measurement (a) along the dipole pole axis and (b) during sideways measurements. The microrobot is 2.5 mm long and 1.25 mm wide. (c) Setup to measure magnetization forces on the microrobot.

data is shown in Fig. 6. The saturation magnetization was measured as $m_s = 4.444 \times 10^5$ A/m.

Next, we measure the forces that the magnet exerts on the assembled-MEMS microrobot. The microrobot is mounted on a plexiglass rod, as shown in Figs. 7(a) and 7(b), which is attached to the force transducer. The magnetic force is measured with a capacitance-based Neonics force transducer instead of the scale. The setup was modified as shown in Fig. 7(c). To precisely position the microrobot, the force transducer is mounted to an MP-285 Motorized Micromanipulator from Sutter Instrument. During the measurements, the long axis of the microrobot is always aligned with the field.

Figure 8 shows the magnetization forces measured on the microrobot. The system provides force data with a desirable signal-to-noise ratio for microrobots at this scale. The curves are qualitatively similar to the ones of the ellipsoid, but the values are orders of magnitude smaller. This force data is utilized in Section III-B.

III. Measuring Hydrodynamic Properties

In order to understand the relationship between applied magnetization force and microrobot velocity, we must understand the hydrodynamic properties of the microrobots. A microrobot in a fluid environment will likely operate at low Reynolds number, where inertial effects are negligible and viscous effects dominate. At low Reynolds number, the microrobot can be assumed to instantaneously reach its terminal velocity, where viscous forces balance the applied magnetic forces [15]. It is possible to analytically determine the hydrodynamic properties of very simple shapes, such as ellipsoids, but we would like to accurately determine the hydrodynamic properties of assembled-MEMS microrobots. For this purpose, we have constructed an experimental setup to measure these effects.

A. Experimental Setup

The microrobot is placed in a fluid-filled vial, as shown in Fig. 9. The position of the microrobot is then tracked with two Basler A602f digital cameras, oriented orthogonally to one another. The magnet is located directly above the vial. The position of the magnet is controlled vertically using the linear stage. A typical screen capture of the computer vision
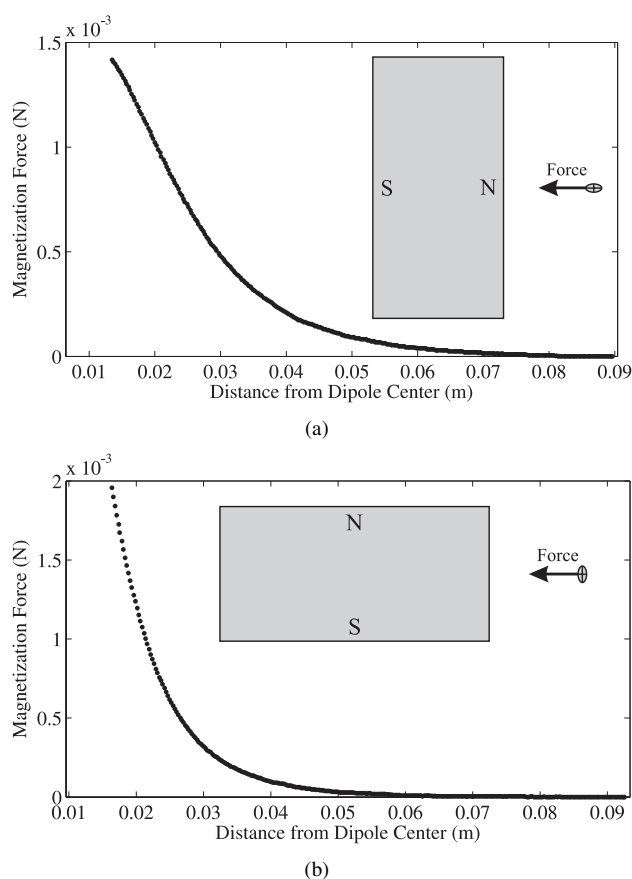
(a)

(b)

Fig. 8. Measured magnetization force on the assembled-MEMS microrobot (a) when approaching the microrobot along the dipole axis of the magnet and (b) when approaching the microrobot sideways. The inset illustrates the experimental setup, drawn with 1:1 scale to the data.
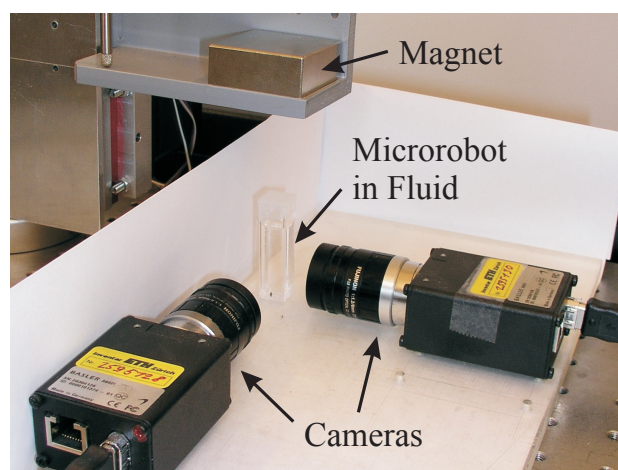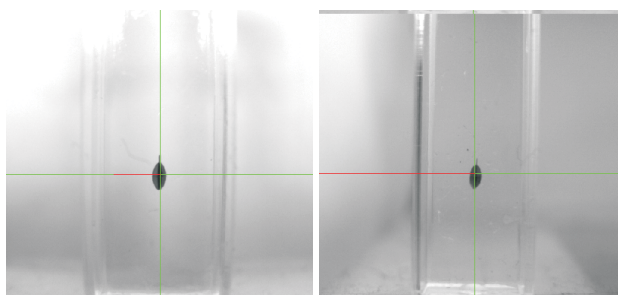

Fig. 9. Experimental setup for measurement of hydrodynamic properties.

Fig. 10. Screen capture of the computer vision system tracking the position of the microrobot in the vial from two sides.

system tracking a microrobot is shown in Fig. 10. The system tracks the center of the microrobot, as indicated in the figure. The microrobot appears dark compared to the surrounding environment, making the tracking robust to lighting levels. For all hydrodynamic experiments in this paper, the vial is filled with AK1000 silicon oil. This oil has a reported density of $970\,\mathrm{kg/m^3}$ and viscosity of $0.98\,\mathrm{Pa\ s}$ at $25\,^\circ\mathrm{C}$. The temperature of the oil during the experiments was $26.9\,^\circ\mathrm{C}$.

B. Microrobot Measurements

Figure 11 shows three runs of data for the microrobot falling under its own weight in silicon oil. For each run, the microrobot is released at the surface of the oil in the vial, and falls to the bottom. The robot tends to right itself in the fluid, so that its long axis is vertical. The data shows how negligible the inertia of the robot really is. The velocity is very constant, and there is no perceived period of acceleration. The data also provides an indication of the noise level in the vision tracking system. In total, six runs of data were collected, with an average velocity of $1.1186\,\mathrm{mm/s}$ and a standard deviation of $0.0123\,\mathrm{mm/s}$.

In the next experiment, the microrobot was positioned at the bottom of the vial. The vial was positioned underneath the magnet so that the long axis of the microrobot was

aligned with the dipole axis of the magnet, yet the attractive magnetic force did not overcome gravity. The gap between the magnet surface and the bottom of the vial was reduced to a constant distance of $60\,\mathrm{mm}$ so the microrobot was pulled toward the magnet. Figure 12(a) shows three runs of distance plotted against time. The closer the microrobot gets to the surface, the stronger the force acting on the microrobot. In Fig. 12(b) the force on the microrobot measured in Section II-D is plotted against velocity, which is obtained by numerical differentiation of the position data with respect to time.

The above data sets are used to compute the coefficient of viscous friction of the microrobot. At low Reynolds numbers, we expect a linear relationship between velocity and viscous drag force in Newtonian fluids [16]:

$$\mathbf{F} = b\mathbf{V} \tag{5}$$

Again, we assume that inertial effects are negligible, such that magnetic forces instantaneously balance viscous forces. We fit a line to the data in Fig. 12(b) through the origin. Note that the measurement obtained from Fig. 11 is represented by a single data point (a square) in Fig. 12(b), and it shows agreement with the linear model. From Fig. 12(b), we compute the coefficient of viscous friction for the microrobot, for motion parallel to the long axis, as $b = 1.41 \times 10^{-2}\,\mathrm{N\cdot s/m}$.
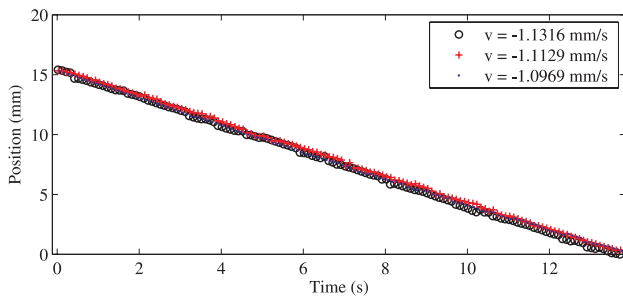
Fig. 11. Three runs of experimental data for microrobot falling under its own weight in AK1000 Silicon Oil.
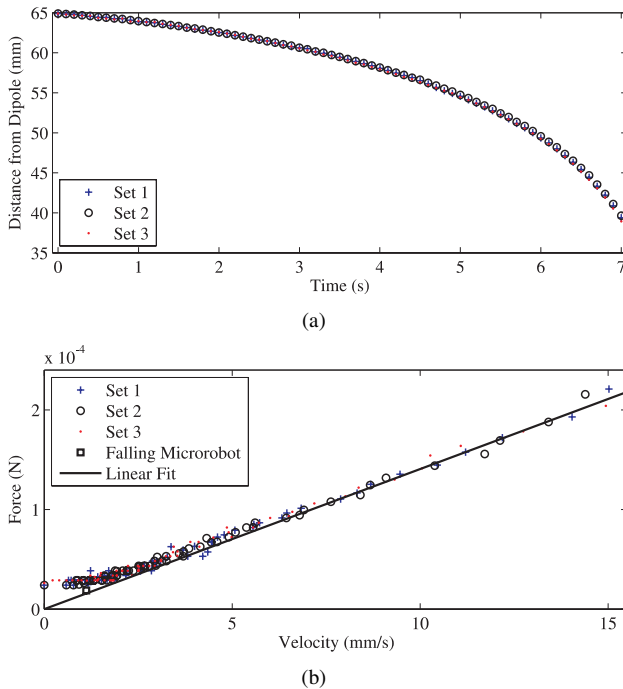

(a)

(b)

Fig. 12. (a) Three runs of distance plotted against time when the microrobot is pulled towards the magnet through AK1000 Silicon Oil. (b) Force plotted against velocity for all data points of postiton data.

IV. Conclusions and Future Work

We have presented a system to measure the magnetic and hydrodynamic properties of assembled-MEMS microrobots in an automated way. Using the system, we determined the magnetic force on a microrobot as a function of the applied magnetic field. We also determined the coefficient of viscous friction of the microrobot in a Newtonian fluid.

We will continue to characterize the magnetic force and viscous drag properties of assembled-MEMS microrobots using the experimental setup presented here. So far we have only investigated the properties of the microrobot in Newtonian fluids. However, we are particularly interested in how microrobots will behave inside the eye. The vitreous humor is the viscoelastic fluid that fills the cavity of the eye [2], and we are currently working towards a simple and inexpensive artificial vitreous humor, based on recent research results [17], that will act as an experimental environment for our microrobots. The experimental system described in this paper will then be used to characterize the hydrodynamic properties of microrobots in the artificial vitreous. These properties can then be used for precise microrobot control in the eye.

References

[1] K. B. Yesin, K. Vollmers, and B. J. Nelson, "Modeling and control of untethered biomicrorobots in a fluidic environment using electromagnetic fields," *Int'l. J. Robotics Research*, vol. 25, no. 5–6, pp. 527–536, 2006.

[2] T. V. Chirila and Y. Hong, "The vitreous humor," in *Handbook of Biomaterial Properties*, J. Black and G. Hastings, Eds. Chapman and Hall, 1998, pp. 125–131.

[3] M. Wautelet, "Scaling laws in the macro-, micro- and nanoworlds," *European J. Physics*, vol. 22, pp. 601–611, 2001.

[4] M. S. Grady, M. A. Howard III, J. A. Molloy, R. C. Ritter, E. G. Quate, and G. T. Gillies, "Nonlinear magnetic stereotaxis: Three-dimensional, in vivo remote magnetic manipulation of a small object in canine brain," *Medical Physics*, vol. 17, no. 3, pp. 405–415, 1990.

[5] G. T. Gillies, R. C. Ritter, W. C. Broaddus, M. S. Grady, M. A. Howard III, and R. G. McNeil, "Magnetic manipulation instrumentation for medical physics research," *Review of Scientific Instruments*, vol. 65, no. 3, pp. 533–562, 1994.

[6] M. B. Khamesee, N. Kato, Y. Nomura, and T. Nakamura, "Design and control of a microrobotic system using magnetic levitation," *IEEE/ASME Trans. Mechatronics*, vol. 7, no. 1, pp. 1–14, 2002.

[7] K. Ishiyama, K. I. Arai, M. Sendoh, and A. Yamazaki, "Spiral-type micro-machine for medical applications," *J. Micromechatronics*, vol. 2, no. 1, pp. 77–86, 2003.

[8] I. Tunay, "Modeling magnetic catheters in external fields," in *Proc. IEEE Int'l. Conf. Engineering in Medicine and Biology Society*, 2004, pp. 2006–2009.

[9] F. Amblard, B. Yurke, A. Pargellis, and S. Leibler, "A magnetic manipulator for studying local rheology and micromechanical properties of biological systems," *Review of Scientific Instruments*, vol. 67, no. 3, pp. 818–827, 1996.

[10] J. J. Abbott, O. Ergeneman, M. P. Kummer, A. M. Hirt, and B. J. Nelson, "A continuous model for magnetization torque on axially symmetric bodies," in *Joint MMM/Intermag Conf.*, 2007, Available Online.

[11] D. Jiles, *Introduction to Magnetism and Magnetic Materials*. London: Chapman and Hall, 1991.

[12] R. C. O'Handley, *Modern Magnetic Materials: Principles and Applications*. New York: John Wiley and Sons, 2000.

[13] M. Beleggia, M. De Graef, and Y. T. Millev, "The equivalent ellipsoid of a magnetized body," *Journal of Physics D: Applied Physics*, vol. 39, pp. 891–899, 2006.

[14] (2007) Princeton Measurements Corporation. [Online]. Available: http://www.princetonmeasurements.com/

[15] E. M. Purcell, "Life at low reynolds number," *American J. Physics*, vol. 45, no. 1, pp. 3–11, 1977.

[16] J. Happel and H. Brenner, *Low Reynolds Number Hydrodynamics*. The Hague: Martinus Nijhoff Publishers, 1983.

[17] C. S. Nickerson, "Engineering the mechanical properties of ocular tissues," Ph.D. dissertation, California Institute of Technology, 2005.